Failure mechanism and design strength of spatial loaded high-strength welded hollow spherical joint

Chen QIU, Jihui XING*,Lina CHENG, Na YANG

* School of Civil Engineering, Beijing Jiaotong University, Beijing 100044, China
jhxing@bjtu.edu.cn

Abstract

Accompanied with the use of high-strength steels, High-performance long-span space frame structures have been developed rapidly nowadays. The design equations for high-strength welded hollow spherical joints (WHSJ) under unidirectional axial load have been established recently. However, the knowledge about the inherent properties of WHSJ under complicated special axial loads, which are obviously different from its unidirectional tension or compression cases, is still quite limited. In this paper, tests on six full-scale in-plane bi-axial loaded joints are reported firstly. The test results are then numerically simulated to validate the finite element (FE) models hereby. Subsequently, the numerical models are extended for spatial loaded WHSJs for further parametric analysis study. The influence of both geometric dimensions and axial force on the bearing capacity of spatial WHSJs are investigated. The research results show that the ratio of axial force, λ_2, between web member and main chord affects the failure mechanism of a spatial loaded joint significantly because of its possible elasto-plastic instability due to the compression state of web members. When the value of λ_2 exceeds 0.7, the failure mechanism of WHSJ with tension and compression main chords tends to be similar. Additionally, the bearing capacity of spatial loaded joints is generally smaller than the design value recommended by the current design guide. Finally, new design formulas for the bearing capacity of spatial loaded high-strength WHSJ are proposed and validated with experimental results for improving the current specification.

Keywords: Welded hollow spherical joint, high-strength steel, spatial load, experiment, numerical simulation, design formula

1. Introduction

Welded hollow spherical joints (WHSJ) have been widely used recently in super-long span structures because of its high stiffness and good seismic performance [1]. The steel ball surface has a complex stress distribution under spatial loading status. However, the previous design specifications are based on unidirectional loading tests [2,3].

With the rapid development of computing power, it is possible to simulate the mechanical behaviors of complex steel joints with the help of numerical simulation techniques. Researchers began to study the multi-directional mechanical properties of WHSJs by means of nonlinear numerical analysis, and the factors affecting these behaviors were also analyzed [4-6]. One group of researchers studied the internal factors, which include geometric dimensions and material properties. Others studied the external factors which include the state of axial forces [6-8]. Whereas, current research on spatial multi-directional loaded WHSJs usually studies joints with in-plane two-way loading configuration. Researchers have paid attention to the influence of the ratio of axial force λ_1 between the branch chord and main chord on joint performance, which will lead to the bearing capacity of the joint being significantly lower than that

Proceedings of the IASS Symposium 2024
Redefining the Art of Structural Design

of the uniaxial loaded joint. Still, the influence of web members has not been considered. In addition, the important influence of geometric discontinuity and material property change caused by ball-chord welding on the bearing capacity of WHSJ is ignored in previous literatures without any test data.

Furthermore, with the increasing demand on high-performance long-span structures, the requirements on the strength of steel are getting higher. High-strength steel can effectively reduce the size of components, reduce the amount of steel and the self-weight of the structure compared with ordinary steel. Study on the mechanical properties of high-strength steel components has attracted great attentions [9]. It is therefore necessary to study systematically the mechanical properties of high-strength WHSJ.

In summary, the biaxial load tests of six full-scale WHSJs were conducted in this paper. A refined three-dimensional solid FE model of the WHSJ specimens was developed in ABAQUS considering the ball-chord weld and its heat-affected zone. The test was numerically simulated to repeat the experimental phenomenon observed. The numerical model originally for bi-axial loaded joints was then extended to model spatially loaded joints. The failure mechanism with the development of plastic zones in the WHSJ under three-dimensional stress conditions was then discussed. The validity of the numerical simulation model for the WHSJ was checked by comparison with experimental results. Parametric analysis on the spatial mechanical performances of WHSJs was then systematically conducted, and design formulas suitable for high-strength WHSJs were proposed and validated for improving the specification (JGJ7-2010) [10].

2. Bearing capacity tests of high-strength WHSJ under in-plane biaxial loads

2.1 Configuration of WHSJ specimens

Due to the limitations of the laboratory, the spatial loading pattern was too difficult to realize and only the in-plane loading state was designed for the test. Six identical high-strength WHSJ specimens were fabricated all of which consisted of a spherical ball and four chord members, as shown in Fig.1. Only 8 mm thick steel plate was available for the study. Therefore, the geometry of the joint was not changed, and only the loading patterns were changed. The hollow ball was processed from 8 mm thick Q460D steel plate. The external diameter and the thickness of the ball are 350 mm and 8 mm, respectively. Both main and branch chords were fabricated from Q460 hot-rolled circular hollow section members with dimensions of Φ114×12 mm, which was slightly thicker than those in practical design to ensure that failure occurred only on the spherical ball.

The internal forces in the branch chord and main chord influence the behavior of the joint significantly. Therefore, different loading patterns were considered in the test scheme. The horizontal chords were taken as the main chords, while the vertical chords were treated as branch chords during the loading process.

Gas-shielded welding with interlayer temperature of 180℃ was adopted. The parameters of the welding procedure are listed in Table 1. The heat input was 15 kJ/cm. And the layers and passes of weld seams for Weld line 1 and Weld line 2 are shown in Fig.1. The specimens were allowed to cool slowly without post-weld heat treatment after welding.

2.2 Mechanical properties of steel materials

A combined stress-strain relationship is considered more reasonable for the post-necking stage according to existing report. Therefore, a widely used Voce-Swift model was adopted:

$$\sigma = (1-w)[k + q(1-e^{-b\varepsilon_p})] + wa(\varepsilon_s + \varepsilon_p)^n \tag{1}$$

where, ε_s is the yield strain of material; ε_p is the plastic strain; Parameters *a, b, k, n, q* and *w* in Eq.(1) can be determined from the material test result, and they are shown in Table 2.

2.3 Test setup

The experimental setup of the test specimens is shown in Fig. 2. Horizontal chords have been assumed as the main chord. One horizontal chord was connected to the horizontal actuator by high-strength bolts

with a hinged connector, while the other horizontal chord was fixed on a wedge-shaped pier fastened to the reaction frame. The bottom of the lower branch chord was fixed to the bottom beam of the loading frame in both cases. The boundary of the top branch chord takes up two forms. When the load in the branch chord was tension, the load was applied by vertical actuator fixed on the upper beam of the frame. The top end of the specimen was fastened to the vertical actuator by high-strength bolts with a hinged connector. Otherwise, the compressive load was applied by a vertical jack above with a sliding support. Once the deformation of the main chords caused horizontal deflection of the upper branch chord, the position of the jack can also be adjusted to provide vertical loading.
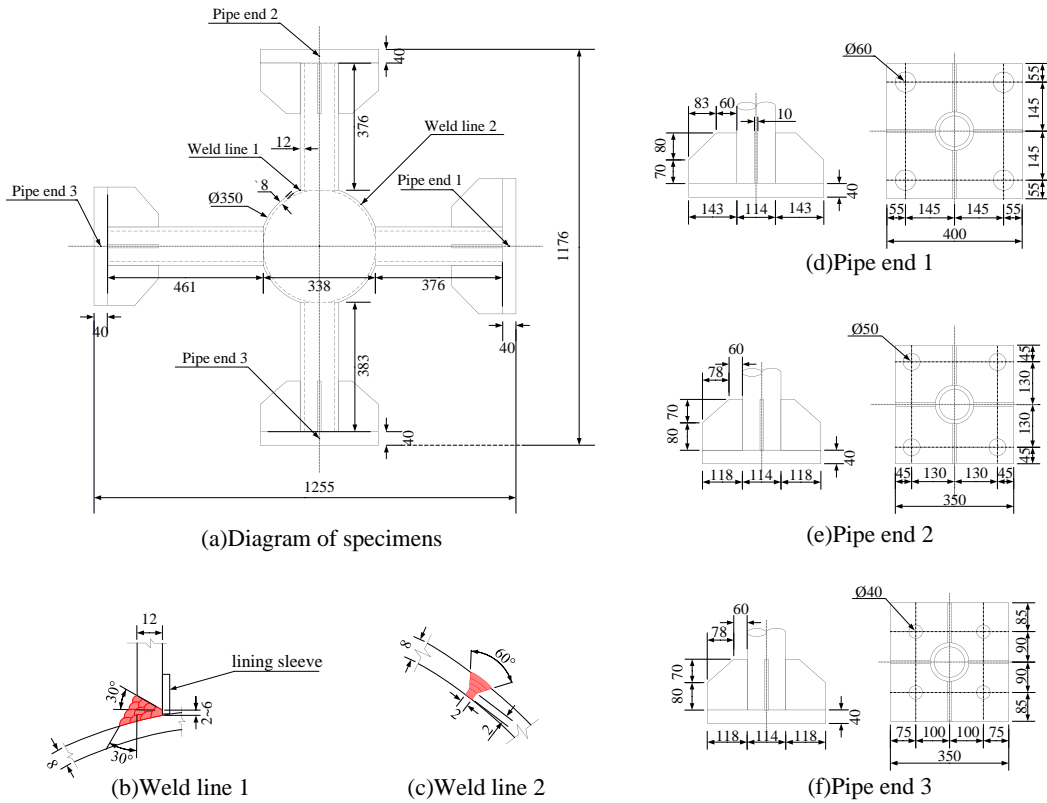

Figure 1: Specimen configuration (Unit: mm)

Table 1: Welding parameters

Wire diameter/mm	Welding process	Polarity	Current/A	Voltage/V	Travel speed/mm·min-1
1.2	SMAW	DCEP	180-260	26-32	200～300

Table 2: Mechanical properties of steel materials

Steel	Elastic modulus E/MPa	Poisson's ratio μ	f_y/MPa	k	q	b	a	n	w
Q460D steel plate	203000	0.3	517	485.3	254.9	20.17	978.2	0.1415	0.75
Weld metal	220000	0.3	474	540.1	281.3	21.32	1067	0.132	0.8
Heat-affected zone	200000	0.3	525	434.5	305.9	19.6	1032	0.171	0.9

There were six different loading patterns for the experiment details of which can be found in Table 3. Constant vertical load was applied to the upper branch chord before horizontal displacement was loaded in the main chord. Loading will continue until failure of the spherical joint.
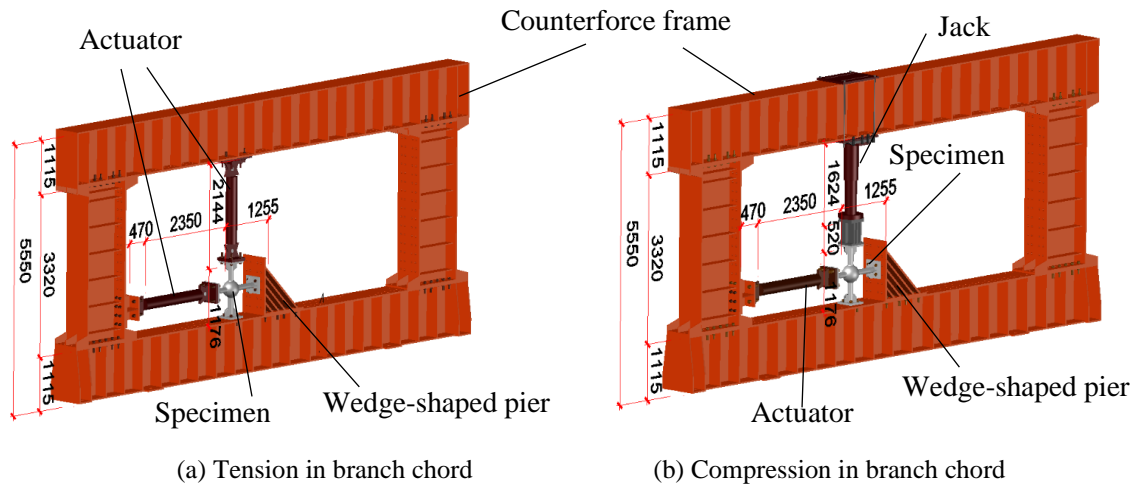
(a) Tension in branch chord (b) Compression in branch chord

Figure 2: Experimental setup

Table 3: Loading patterns of all specimens

Specimen ID	Loading pattern	Force applied to branch chord/t
C-C-40	Biaxial compression	40
T-T-40	Biaxial tension	40
C-T-40	Compressive main chord and tensile branch chord	40
T-C-40	Tensile main chord and compressive branch chord	40
C-C-60	Biaxial compression	60
T-C-60	Tensile main chord and compressive branch chord	60

3. Experimental results

3.1 Experimental phenomena

The failure of WHSJs with the same type of force in the main chord is very similar. Common failure mode for WHSJ with compressive main chords is shown in Fig.3, while typical failure mode for WHSJ with tensile main chords is illustrated in Fig.4. Specimen with compression main chords had local cave-in at the intersection area of the loaded main chord and the spherical ball. Then the indented area became larger with increasing load in the main chords, until a circular belt of case-in area occurred on the ball, as shown in Fig.3(c). Once the ultimate load bearing capacity was achieved, yielding of material and large deformation of the ball surface occurred rapidly.

(a)Initial status   (b) Local cave in   (c)Larger cave-in area   (d) Residual deformation
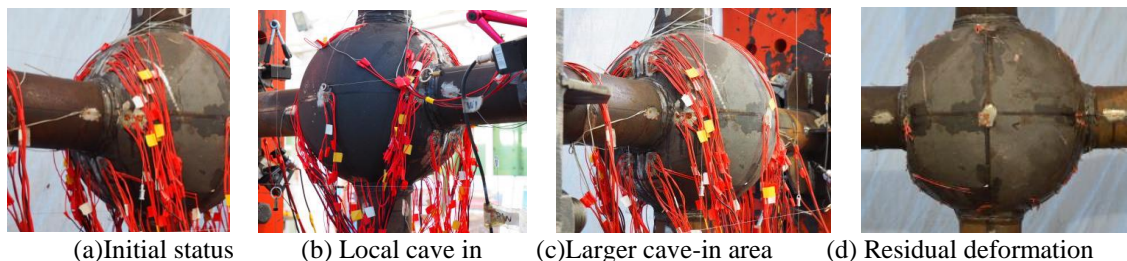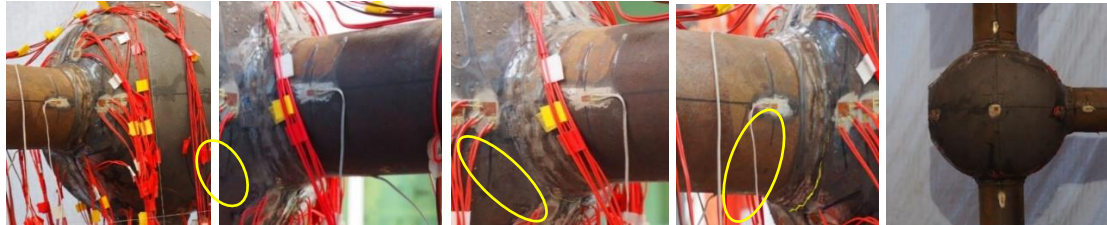
Figure 3: Failure mode of Specimen C-C-60

For specimens with tensile main chords, local yielding due to uneven stress distribution occurred at the heat-affected zone (HAZ), which was very close to the weld seam between the loaded main chord and the spherical ball. Plasticity developed fully along the HAZ at the main chord-to-ball intersection line, leading to the initiation of fracture, as shown in Fig.4(b). Fracture propagated rapidly along the circular

yielded belt (Fig.4(c)). After the entire section was weakened by a certain critical extent (Fig.4(d)), rupture occurred accompanied with a sudden loud noise. The whole spherical ball changed slightly to a date-nucleus shape due to the elongation along the horizontal main chord direction.


(a)Initial status (b)Fracture initiation (c)Fracture propagation (d)Before rupture (e)Residual deformation

Figure 4: Failure mode of Specimen T-C-60

In short, the failure modes of the two types of joints with tension or compression in the main branch under in-plane biaxial loading are significantly different, but they are similar to the failure modes under uniaxial loading [11].

3.2 Load-displacement curves

The load-displacement curves for all six specimens are plotted in Fig.5. Responses of specimens from different loading patterns are compared in Fig.5(a). The WHSJs with tension main chords are shown to have higher resistance but lower stiffness than WHSJs with compression main chords. This indicates that the direction of the internal forces in the main chords has significant influence on the biaxial loading bearing capacity of the WHSJ. The direction of branch force has slight effect on the bearing capacity of the joint, but it has significant impact on its stiffness. WHSJ subjected to biaxial compression loads provides the worst ultimate strength. The responses of specimens to large or small branch forces are compared in Fig.5(b). It can be concluded that WHSJs with higher branch forces have poorer load bearing capacities when the main chord is tensile. This is reversed when the main chord is compressive.
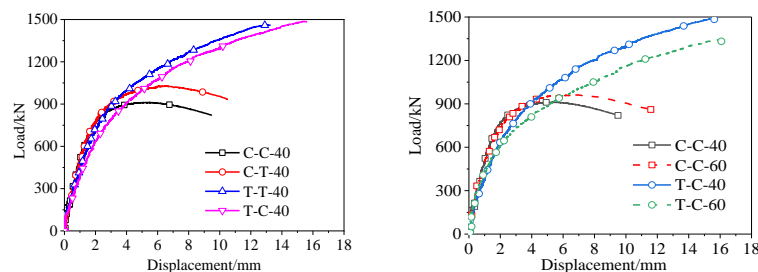
(a) Specimens under different biaxial load patterns   (b) Specimens subjected to different branch force

Figure 5: Effect of different load patterns

4. Numerical analysis on the experimental specimens

4.1 FE models of the WHSJs

FE analysis on the experimental joints was conducted in ABAQUS to reproduce the test results and phenomenon observed in all specimens. The biaxial loaded WHSJ specimens were modelled using three-dimensional C3D8R solid elements. The welded zone and HAZ are also included in the FE model. The geometry and dimensions of the chord-to-ball welded zone were determined according to the real shape of the weld in the test specimens. But the lining sleeve shown in the upper left corner of Fig.1 was not modelled due to difficulties to define its additional stiffness to the ball. The range of the HAZ was taken as 1.5 times the thickness of the ball thickness. Additionally, a constant 0.5 mm was taken as the negative tolerance of the wall thickness when referring to the sensitive analysis for specimens.

Typical 3D FE model of the WHSJ specimens is illustrated in Fig.6(a). Most elements were hexahedral elements, while a small number of wedge-shaped or triangular elements were allowed. A sufficiently

refined mesh element size of 0.25 mm was adopted near the chord-to-ball connection regions (in Fig.6(b)), where fracture or surface cave-in phenomena were anticipated to happen. Coarse mesh size of roughly 5 mm was used in other parts of the joint, such as the end plates, stiffener ribs, chord members and middle part of the spherical ball, etc. The number of elements within the thickness of the ball was four based on the sensitivity analysis results.

All degrees-of-freedom (DoFs) at the loading end of the main chord and branch chord were coupled by kinematic coupling technique with the DoFs of two reference points RP-1 and RP-2, which is loacted at 300 mm and 400 mm away from the end plates respectively. Boundary constraints were provided as shown in Fig.6(c). Axial load was applied to the main chords by giving a horizontal displacement at the reference point RP-2 of the FE model, then vertical force was applied on the branch chord. Both geometrical and material nonlinearities were considered in the numerical simulation. And the static Riks method was employed to study the mechanical behavior of the experimental WHSJs.
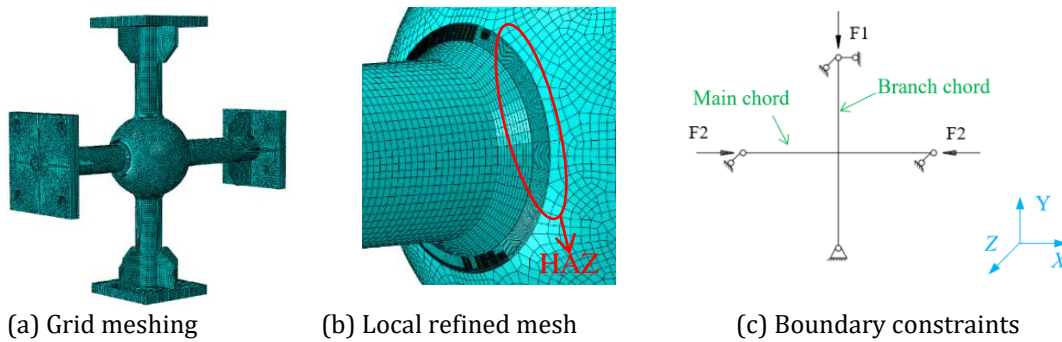

(a) Grid meshing   (b) Local refined mesh   (c) Boundary constraints

Figure 6: 3D Finite-element model of WHSJ specimens

4.2 Analysis results

All load-displacement curves from both the experimental specimens and numerical models are plotted in Figs.7(a) and (b). It is noted that they were in good agreement for joints with tensile main chords. The maximum difference of the ultimate bearing capacity was 16.9% for specimen T-C-60. However, simulated ultimate bearing capacities for joints with compressive main chords were lower than the test results. This may be due to the difficulty to model the lining sleeve in the numerical analysis. Although the sleeve was not welded directly to the spherical ball as shown in Fig.1, yet any components perpendicular to the spherical surface could provide effective out-of-plane stiffness to the buckling of the surface, resulting in an improved compressive resistance of the joint.
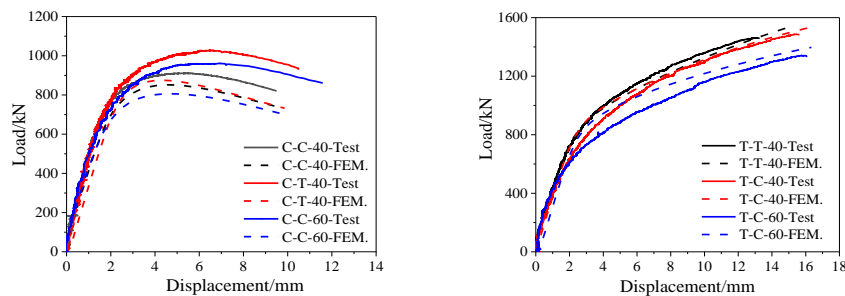
(a) Specimens with main chord under compression   (b) Specimens with main chord under tension

Figure 7: Comparison of load-displacement curves

4.3 Failure mechanism of WHSJs under biaxial load

Typical experimental and numerical failure modes of WHSJ subjected to biaxial loads are shown in Fig.8. Good agreement can also be observed for the typical C-C-40 and T-T-40 specimens.

Failure mode of C-C-40 displayed in Fig.8(a) was particularly common in specimens with compressive main chords. The development of plastic strains in the ball and corresponding load-displacement curve are also shown in Fig.8 (a). It can be ovserved that plastic strain appears at the internal ball surface far

from the intersection of the ball and chord (Point A in Fig.9(a)).Then the external surface at the toe of the chord-to-ball weld yielded (Point B in Fig.9(a)). Then plasticity in the ball thickness increased gradually leading to a degradation of the joint stiffness, until the joint reached its ultimate bearing capacity (Point C in Fig.9(a)). It should be noted that the plasticity has not yet been fully developed throughout the wall thickness of the ball. Two yielded regions at the internal and external surfaces of the ball wall were independent to each other as shown. Whereas, the ultimate bearing capacity of the joint declined sharply. Deformation of the ball increased notably, resulting in rapid plasticity development in the wall and two yielded regions merged. This failure processof the biaxial loaded WHSJ with compressive main chord may suggest an elasto-plastic buckling.
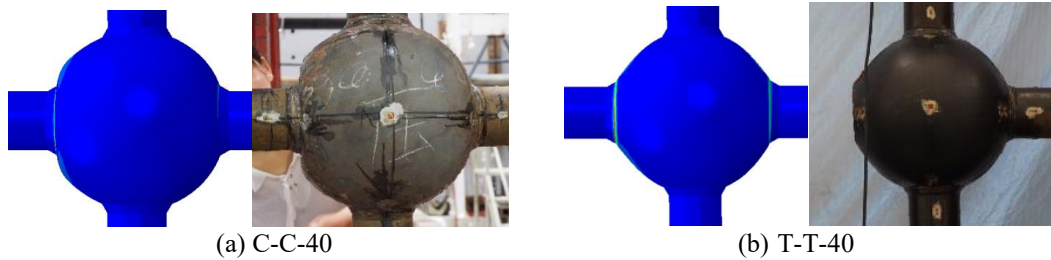

(a) C-C-40   (b) T-T-40

Figure 8: Typical failure modes of specimens
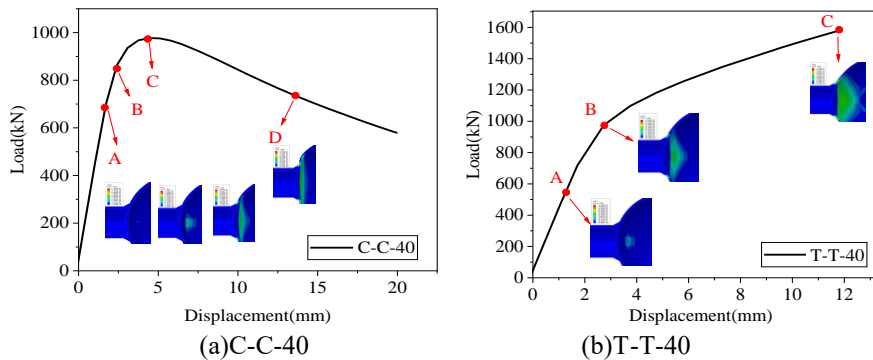

(a)C-C-40   (b)T-T-40

Figure 9: Development of plastic strain in the spherical ball

Failure mode of specimen T-T-40 in Fig.8(b) was common for WHSJs with tensile main chords. The development of its plastic strains and corresponding load-displacement curve is illustrated in Fig.9(b). It can be seen that the initial yielded state of WHSJ in Fig.9(b) was similar to that in Fig.9(a). With the increase of axial force in the main chords, steel at the chord-to-ball weld toe yielded. This corresponds to point B in Fig.9(b). The stiffness of the joint decreased significantly with further load. Plasticity increased gradually in the wall of the ball, especially around the chord-to-ball weld toe. When plasticity was fully developed throughout the thickness of the wall of ball, as shown in Fig.9(b), plastic hinge occurred at the HAZ around the intersection of ball and chord, with the joint reaching its ultimate bearing capacity. Therefore, the failure mechanism of the in-plane biaxial loaded WHSJ with tensile main chord was typical punching failure.

It may be concluded, in general, that the FE models developed for this study were able to accurately replicate the nonlinear behaviors of WHSJs fabricated from Q460 high-strength steel in the in-plane biaxial loaded experiments. These models were considered suitable for further numerical simulation and parametric studies.

5. Study on the spatial mechanical properties of WHSJ

5.1 Loading pattern

A typical WHSJ in plate pyramid grid-latticed structure shown in Fig.10 was taken as an example. Four orthogonal chord members were arranged in the horizontal plane, and four web members were

intentionally designed to have the same angle with the horizontal plane. Two of the chords carried the largest axial force F, while the other two chords carried slightly smaller internal force, λ_1F. By adjusting the ratio of the axial force between the main chord and branch chord, $\lambda_1(0\leq\lambda_1\leq1.0)$, the proportion of the axial force in the branch chord could be controlled. However, the internal force in all web members were in a state of equilibrium with the rest of the joint. Therefore, the simplest way was to have the internal force of all web members assigned the same value, λ_2F but in mutually different directions. Coefficient λ_2 was the ratio of axial force between the web member and the main chord, and its value could be controlled with $0<\lambda_2\leq1.6$. The ends of chord members were restrained with pin supports while the ends of all web members were free in the computation model of the joint.
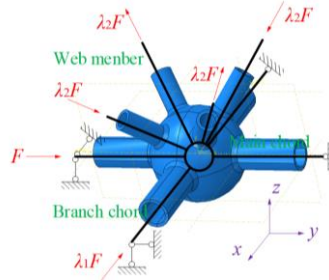

Figure 10: Schematic diagram of the spatial loading pattern for WHSJ

Additionally, the same size for all chords and web members are designed hereby to avoid too many parameters considered in the numerical study. The boundary effect in the analysis could also be reduced by taking the length of each member as 2.0 times of its external diameter [11]. Material parameters in Table 3 were adopted. The FE modeling of the spatial WHSJ were prepared similar to that described in Section 4.1.

Based on initially parameteric analysis results for few WHSJs, the bidirectional compression loading was taken as the standard loading scenario of WHSJ when its main chord is under compression, while tension-and-compression loading was taken as the standard loading scenario to determine the bearing capacity of a WHSJ when the main chord is under tension.

5.2 Parametric analysis scheme of spatially loaded WHSJs

The main factors affecting the bearing capacity of WHSJs are: the hollow ball diameter D, wall thickness of ball T, chord diameter d, wall thickness of chord t, angle between the web members and chord plane θ, and the ratio of axial force λ_1 between the main chord and branch chord and the ratio of axial force λ_2 between the web members and the main chord, and whether the ball is ribbed or not. A total of 58 computational models on the WHSJ were designed and 116 sets of results are obtained from numerical simulation. Detailed information on these 58 specimens is given in Table 4, where "-R" in the model ID denotes the spherical ball had rib on the internal surface of the ball.

Table 4: Model ID and parameters for different computation models

Code No.	Model ID	D/mm	T/mm	d/mm	t/mm	D/T	D/d	T/t	$\theta/°$	λ_1	λ_2	Rib stiffener
1	JD1	200	8	89	6	25.00	2.25	1.33	60	0.6	0.4	×
2	JD2	250	8	89	6	31.25	2.81	1.33	60	0.6	0.4	×
3	JD3	300	8	89	6	37.50	3.37	1.33	60	0.6	0.4	×
4	JD4	450	16	219	12	28.16	2.05	1.33	60	0.6	0.4	×
5	JD5	600	16	219	12	37.50	2.74	1.33	60	0.6	0.4	×
6	JD6	750	16	219	12	46.88	3.42	1.33	60	0.6	0.4	×
33	JD4-R	450	16	219	12	28.16	2.05	1.33	60	0.6	0.4	√
34	JD5-R	600	16	219	12	37.50	2.74	1.33	60	0.6	0.4	√
35	JD6-R	750	16	219	12	46.88	3.42	1.33	60	0.6	0.4	√
36	JD7-R	600	12	194	10	50.00	3.09	1.20	60	0.6	0.4	√
37	JD8-R	600	14	194	10	42.86	3.09	1.40	60	0.6	0.4	√
38	JD9-R	600	16	194	10	37.50	3.09	1.60	60	0.6	0.4	√

39	JD10-R	600	18	194	10	33.33	3.09	1.80	60	0.6	0.4	√
7	JD11	450	12	168	10	37.50	2.68	1.20	60	0.6	0.4	×
8	JD12	450	14	168	10	32.14	2.68	1.40	60	0.6	0.4	×
9	JD13	450	16	168	10	28.16	2.68	1.60	60	0.6	0.4	×
10	JD14	450	18	168	10	25	2.68	1.80	60	0.6	0.4	×
40	JD11-R	450	12	168	10	37.50	2.68	1.20	60	0.6	0.4	√
41	JD12-R	450	14	168	10	32.14	2.68	1.40	60	0.6	0.4	√
42	JD13-R	450	16	168	10	28.16	2.68	1.60	60	0.6	0.4	√
43	JD14-R	450	18	168	10	25	2.68	1.80	60	0.6	0.4	√
11	JD15	450	14	133	10	32.14	3.38	1.40	60	0.6	0.4	×
12	JD16	450	14	152	10	32.14	2.96	1.40	60	0.6	0.4	×
13	JD17	450	14	194	10	32.14	2.32	1.40	60	0.6	0.4	×
14	JD18	450	14	219	10	32.14	2.05	1.40	60	0.6	0.4	×
44	JD15-R	450	14	133	10	32.14	3.38	1.40	60	0.6	0.4	√
45	JD16-R	450	14	152	10	32.14	2.96	1.40	60	0.6	0.4	√
46	JD17-R	450	14	194	10	32.14	2.32	1.40	60	0.6	0.4	√
47	JD18-R	450	14	219	10	32.14	2.05	1.40	60	0.6	0.4	√
48	JD19-R	600	22	219	12	27.27	2.74	1.83	60	0.6	0.4	√
49	JD20-R	600	22	219	14	27.27	2.74	1.57	60	0.6	0.4	√
50	JD21-R	600	22	219	18	27.27	2.74	1.22	60	0.6	0.4	√
15	JD22	450	14	168	9	32.14	2.68	1.56	60	0.6	0.4	×
16	JD23	450	14	168	12	32.14	2.68	1.17	60	0.6	0.4	×
17	JD24	450	22	152	14	20.45	2.96	1.57	50	0.6	0.4	×
18	JD25	450	22	152	14	20.45	2.96	1.57	60	0.6	0.4	×
19	JD26	450	22	152	14	20.45	2.96	1.57	70	0.6	0.4	×
20	JD27	300	12	114	10	25.00	2.63	1.20	60	0.2	0.4	×
21	JD28	300	12	114	10	25.00	2.63	1.20	60	0.4	0.4	×
22	JD29	300	12	114	10	25.00	2.63	1.20	60	0.6	0.4	×
23	JD30	300	12	114	10	25.00	2.63	1.20	60	0.8	0.4	×
24	JD31	300	12	114	10	25.00	2.63	1.20	60	1.0	0.4	×
51	JD32-R	600	22	219	14	27.27	2.74	1.57	60	0.2	0.4	√
52	JD33-R	600	22	219	14	27.27	2.74	1.57	60	0.4	0.4	√
53	JD34-R	600	22	219	14	27.27	2.74	1.57	60	0.8	0.4	√
54	JD35-R	600	22	219	14	27.27	2.74	1.57	60	1.0	0.4	√
25	JD36	300	12	114	10	25.00	2.63	1.20	60	0.6	0.7	×
26	JD37	300	12	114	10	25.00	2.63	1.20	60	0.6	1.0	×
27	JD38	300	12	114	10	25.00	2.63	1.20	60	0.6	1.3	×
28	JD39	300	12	114	10	25.00	2.63	1.20	60	0.6	1.6	×
55	JD40-R	600	22	219	14	27.27	2.74	1.57	60	0.6	0.7	√
56	JD41-R	600	22	219	14	27.27	2.74	1.57	60	0.6	1.0	√
57	JD42-R	600	22	219	14	27.27	2.74	1.57	60	0.6	1.3	√
58	JD43-R	600	22	219	14	27.27	2.74	1.57	60	0.6	1.6	√
29	JD44	200	10	60	6	20.00	3.33	1.67	60	0.6	0.4	×
30	JD45	200	10	68	6	20.00	2.94	1.67	60	0.6	0.4	×
31	JD46	200	10	73	6	20.00	2.74	1.67	60	0.6	0.4	×
32	JD47	200	10	83	6	20.00	2.41	1.67	60	0.6	0.4	×

5.3 Mechanical behavior and failure mechanism of spatial loaded WHSJs

In order to compare with in-plane biaxial loaded WHSJ, a new spatial loaded WHSJ model was designed for this study with the same geometry as the experimental specimens in section 2. Four new Φ114×12 mm web members were added to the FE model for the experimental specimens. WHSJ with tensile main chords was taking as an example to investigate the development of plastic strain in the spatial loaded WHSJ. The loading patterns were the same as described in Section 5.1. The values of λ_1 and λ_2 were assumed to be 0.6 and 0.4, respectively. The main features of the plastic strain development in the ball and corresponding load-displacement curve are illustrated in Fig.11.

As shown in Fig.11(b), plasticity firstly developed at the HAZ close to the main chord-to-weld connection. The horizontal stiffness of the WHSJ was slightly reduced as a result, and the slope of the loading-displacement curve changed slightly (see point A in Fig.11(a)). Then the HAZ at the root of the

tensile web member, which was near the plastic region, also yielded as shown in Fig.11(c). The transmission of stress along the surface of the ball was no longer smooth and the stiffness of the ball was seriously weakened, leading to notable change in the load-displacement curve (see point B in Fig.11(a)). When the ultimate bearing capacity of the WHSJ was reached, plasticity had not yet fully developed, as shown in Fig.11(d), to form a belt of interconnected plastic hinge in the ball surface. However, there was a concentration of plastic strain at the HAZ at the root of the compressive web member. This may be due to the local elasto-plastic buckling of the ball surface. Then the ultimate bearing capacity of the joint dropped sharply (point C in Fig.11(a)). End displacement of the main chord was small and less than 4 mm, and there was no fracture initiated in the HAZ around the main chord-to-weld connection. Therefore, the joint could still take up tension from the main chord, and its load-displacement curve even rose slightly. Finally, a notable belt of cave-in area occurred around the compressive web member-to-ball intersection region, as shown in Fig.11(e).

(a) Load-displacement curve

(b) HAZ of main chord-to-ball connection yield

(c) HAZ of web member-to-ball connection yield

(d) Under ultimate load

(e) Large plastic deformation developed around the root of the web member
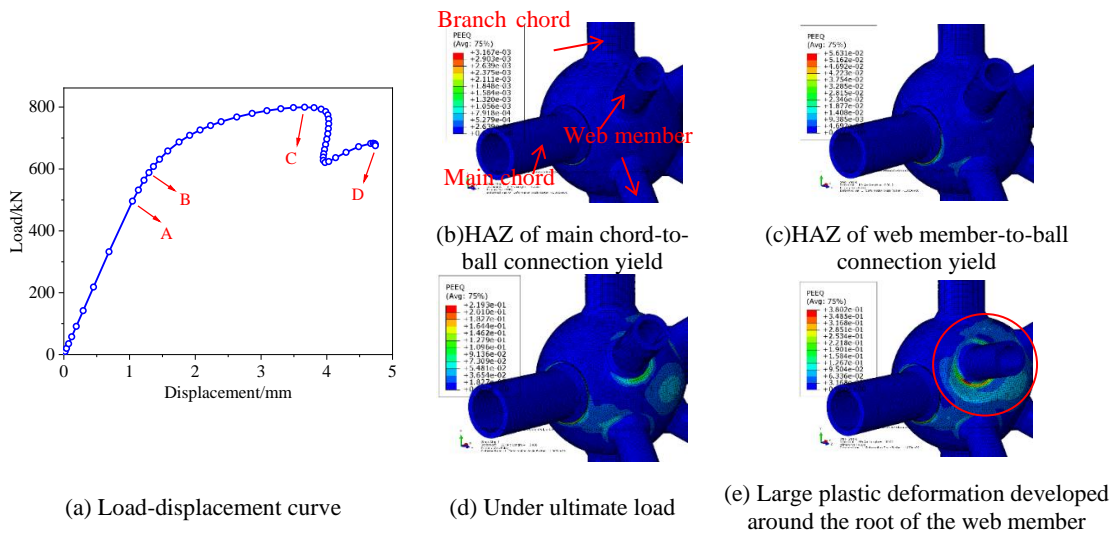
Figure 11: Typical response of spatial loaded WHSJ with tension main chords

Comparison between Figs.9(b) and 11 shows that the failure mechanism of a spatial loaded WHSJ is quite different from that of WHSJ under in-plane biaxial loads. Both elasto-plastic buckling and tensile failure may occur during the collapse process of the spatially loaded WHSJ with the main chords in tension. The joint may get damaged due to the cave-in of the HAZ at the root of the web member or fracture of the main chord. Furthermore, in order to clearly understand the influence of different loading patterns on the failure mechanism of a WHSJ, the load-displacement curves of the WHSJ specimens under uniaxial load, in-plane biaxial loads and spatial loads are compared in Fig.12. It is noted that the ultimate bearing capacity of spatial loaded WHSJ with tension main chords is only 54.3% that of uniaxial loaded WHSJ with different failure mechanisms. Although the spatial loaded cases with compressive main chords are also damaged from elasto-plastic buckling, its ultimate bearing capacity is 15.16% lower than that of uniaxial compressive WHSJ owing to its complex stress state.

6. New design equations for High-strength WHSJ

Based on parametric analysis results, the new proposed design equations for WHSJs are obtained as:

$$N_t = \eta_\lambda \eta_R (1.032 + 39.63 \frac{Td}{D^2}) Tdf \tag{2}$$

$$N_c = \eta_\lambda \eta_R (0.865 + 52.56 \frac{Td}{D^2}) Tdf \tag{3}$$

where N_t and N_c are the design bearing capacities for joints with tensile and compressive main chords, respectively. f is the design strength of the material; η_R is the amplification factor from the internal ribs of the stiffened ball, and it equals to 1.0 when there is no internal rib; η_λ is a coefficient accounting for the effects of λ_1 and λ_2.

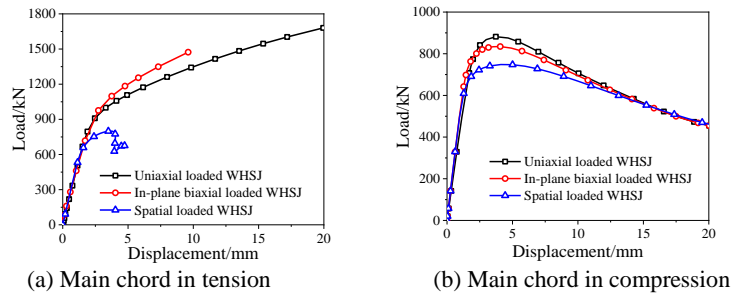| (a) Main chord in tension | (b) Main chord in compression |

Figure12: Comparison of load-displacement curves of joints under different loads

The safety factor on the design bearing capacity in Eqs. (2) and (3) is taken as 1.6, which is the same as that for WHSJ in the JGJ 78-91 in China. The amplification factor η_R for WHSJ with the main chords in tension and compression are taken as 1.08 and 1.04, respectively. And the influence coefficients of the axial force ratios, η_λ, is assumed to take up a quadratic polynomial of the axial force ratios as:

$$\eta_\lambda = 1.665 - 0.1196\lambda_1 - 1.754\lambda_2 + 0.5863\lambda_2^2 \tag{4}$$

The maximum difference between the predictions from the proposed formulas and the FE analysis results for WHSJ models with tensile and compressive main chords are less than 15.1% and 7.5%, respectively.

7. Conclusion:

The failure mechanisms and bearing capacity of high-strength spatial loaded WHSJ have been systematicly investigated in this study. It can be concluded that the failure mechanism of the WHSJ with tensile main chords under spatial loads is significantly different from that of the joint under uniaxial or biaxial tensile loads. The failure mode is affected greatly by the compression state of the web member with the phenomena of elasto-plastic instability and tensile failure of the joint. The bearing capacity and ductility of the WHSJs are greatly reduced. The failure mechanism of joints with compressive main chord is similar to that of in-plane biaxial loaded joints with elasto-plastic instability and an associated reduced bearing capacity. Additioally, new design formulae on the bearing capacity of high-strength WHSJ is proposed according to the failure mechanism of spatially loaded joints studied. Comparison with limited numerical predictions by other researchers shows a mean and standard deviation of the prediction error of 5.58% and 2.89% respectively.

Acknowledgements

References

[1] B. Ding, Y. Zhao, Z. Huang, *et al*. , "Tensile bearing capacity for bolted spherical joints with different screwing depths of high-strength bolts," *Engineering Structures*,vol. 225, 111255, 2020.

[2] X. Xu, T. Shu, J. Zheng, *et al*., "Experimental and numerical study on compressive behavior of welded hollow spherical joints with external stiffeners," *Journal of Constructional Steel Research*, vol.188, 107034, 2022.

[3] B. Huang, M. Lu, Y. Cao, *et al.*, "Experimental study on residual performance of welded hollow spherical joints subjected to axial compression after a fire, " *Structures*, vol. 30, no. 4, pp. 996-1005, 2021.

[4] W. Luan, "The research on ultimate bearing capacity of large-scale welded hollow spherical joint, " Lanzhou: Lanzhou University of Technology, 2011. [In Chinese]

[5] X.F. Yuan, Z.L.Peng, S.L.Dong, "Load-carrying capacity of welded hollow spherical joints subject to combined planar tri-directional axial force and bending moment, " *Journal of Zhejiang University (Engineering science)*, vol.41, no.9, pp.1436-1442, 2007. [In Chinese]

[6] H.J. Tang, "Load-carrying capacity and practical calculation method of welded hollow spherical subject to combined axial force and bending moment, " Hangzhou: Zhejiang University, 2005. [In Chinese]

[7] K.Q.Yu, J.T. Yu, B.Tang, "Experimental and finite element analysis on the ultimate bearing capacity of hollow spherical joints with ribbed stiffener, " *Industrial Construction*, vol.41, no.8, pp. 85-90, 2011. [In Chinese]

[8] F. Wang, X.Wang, C.H. Sun, "FEM analysis of stiffness of welded spherical joint under bi-directional loads, " *Journal of Ningbo University of Technology*,vol. 27, no.2, pp. 15-19, 2015. [In Chinese]

[9] X. Meng, L. Gardner , "Testing, specimenling and design of normal and high strength steel tubular beam-columns, " *Journal of Constructional Steel Research*,vol.183, 106735,2021.

[10] China Academy of Building Research, "Technical Specification for Space Frame Structures (JGJ 7-2010), " Beijing: China Architecture & Building Press, 2010. [In Chinese]

[11] J. Xing, C. Qiu, M. Wang, *et al*, " Uniaxial failure mechanism and design strength of high-strength welded hollow spherical joint, " *Engineering structures*,vol. 256, 113897, 2022.

[12] L.N. Cheng, Research on biaxial loading of welded hollow spherical joint based on Q460 high strength steel. Beijing: Beijing Jiaotong University,2019. [In Chinese]